Combining the thick level set method with plasticity

Mororó, L. A.T.; van der Meer, F. P.

DOI
10.1016/j.euromechsol.2019.103857

Publication date
2020

Document Version
Accepted author manuscript

Published in
European Journal of Mechanics, A/Solids

Combining the Thick Level Set method with plasticity

L.A.T. Mororó[a,b], F.P. van der Meer[b]

[a] *Federal Institute of Education, Science and Technology of Ceará, Morada Nova, Brazil*
[b] *Delft University of Technology, Faculty of Civil Engineering and Geosciences, PO Box 5048, 2600 GA Delft, The Netherlands*

Abstract

The Thick Level Set (TLS) method has been proposed as a new approach to the modeling of damage growth in solids. The fronts of damaged zones are implicitly represented as a level set of an auxiliary field whose evolution is accomplished by the level set method. The TLS model contains a characteristic length to obtain a non-local description that prevents spurious localization in the strain field. The update of the damage is indirectly performed by integrating local values of energy release rate over this characteristic length. This model offers an automatic transition from damage to fracture, and deals with merging and branching cracks as well as crack initiation in an easy and robust manner. In this paper, the TLS is applied to simulate the formation of cusps in a polymer matrix loaded in shear. Realistic simulation of this process requires the damage model to be combined with plasticity in order to capture the behavior of the material prior to failure. To accommodate for plasticity, several changes to the TLS framework are introduced. A strength-based criterion for initiation of damage based on the ultimate yield surface of such plasticity model is proposed. A mapping operator for transferring history is included if the integration scheme in element changes. Furthermore, a new loading scheme is devised that does not rely on secant unloading. Numerical experiments demonstrate the accuracy and effectiveness of the proposed model to handle simulation of crack growth in a medium with hardening plasticity.

Keywords: Thick Level Set, Ductile fracture, Plasticity, Mode II loading, Polymer matrix

Email addresses: l.a.taumaturgomororo@tudelft.nl/luiz.mororo@ifce.edu.br (L.A.T. Mororó), f.p.vandermeer@tudelft.nl (F.P. van der Meer)

1. Introduction

The Thick Level Set (TLS) method to model damage in solids was originally proposed by Moës *et al.* [1, 2]. In the TLS, the location of the front of a damaged zone is implicitly represented as the zero level set of an auxiliary field and its evolution is handled with the level set method [3, 4]. Unlike conventional continuum damage models, in which the damage variable is a direct function of the local strain field, the TLS considers a band of damage with a predefined characteristic length where the damage variable depends on the level set value whose evolution is dictated by the non-local strain field. Macro-cracks, i.e. regions with damage equal to one, appear as a consequence of the front evolution. As the damage evolution is separated from computation of displacement [2, 5], the TLS is a robust method which can handle multiple branching and merging cracks without convergence problems.

Since the first paper on the TLS [1], improvements on its implementation have been proposed [2, 6] and more recently an extension was presented, where the main idea is to couple cohesive zone models with the TLS to capture crack opening [7]. In other publications, the TLS has been compared with alternative approaches, such as phase-field [8] and cohesive zone [9] models.

One application where the robustness of the TLS is particularly relevant is the simulation of cusp formation, which involves many merging cracks. Cusp formation is a process that accompanies mode II delamination crack growth and it is understood to be one of the causes of the difference in fracture energy between mode I and mode II crack growth [10, 11, 12]. This process starts with an array of inclined cracks which are perpendicular to the direction of maximum principal stress. As these cracks evolve, S-shaped cracks are formed, which eventually merge, leading to a single crack on a higher level of observation. Appropriate theoretical and computational tools that can predict this process on the microscale may lead to a better understanding of the mechanisms behind the observed variability in fracture energy, which may in turn allow for devising physics-based criteria [10, 11].

When loaded in shear, polymers behave plastically prior to failure. Therefore, plasticity cannot be ignored in simulation of cusp formation. However, adding plasticity to the TLS is not a straightforward task, because the current solution procedure [2, 5] depends on the assumption of secant unloading

behavior.

This work seeks to simulate the cusp formation process more realistically. For this purpose, the TLS method in the version by Van der Meer and Sluys [5] is extended with a plasticity formulation. To represent the plastic behavior of polymers, the pressure-dependent plasticity model by Melro *et al.* [13] is implemented in the TLS framework. A plasticity-related criterion for damage initiation is introduced and a new loading scheme is devised that does not rely on secant unloading.

The paper is structured as follows. Section 2 is devoted to the formulation of the proposed model, presenting the plasticity model, recalling some fundamentals of the TLS damage model and detailing the main features added to the framework from Van der Meer *et al.* [5]. Several numerical examples including plasticity are presented in Section 3 and used to assess the accuracy of the proposed model to deal with cusp formation. Finally, conclusions are presented in Section 4.

2. Model formulation

2.1. Separation between damage and plasticity

In this section, the main features of the proposed model are outlined. The quasi-static problems that are assessed in this work are based on the framework of small displacements and additive decomposition of the total strain $\boldsymbol{\varepsilon}$ into an elastic (or reversible) part $\boldsymbol{\varepsilon}^{\mathrm{e}}$ and a plastic (or permanent) part $\boldsymbol{\varepsilon}^{\mathrm{p}}$:

$$\boldsymbol{\varepsilon} = \boldsymbol{\varepsilon}^{\mathrm{e}} + \boldsymbol{\varepsilon}^{\mathrm{p}} \tag{1}$$

The equilibrium equation and the relation between the total strain $\boldsymbol{\varepsilon}$ and the displacement field $\mathbf{u}$ in a body Ω without body force read, respectively:

$$\nabla \cdot \boldsymbol{\sigma} = 0 \quad \text{and} \quad \boldsymbol{\varepsilon} = \frac{1}{2}\left(\nabla \mathbf{u} + \nabla \mathbf{u}^{\mathrm{T}}\right) \tag{2}$$

in which $\boldsymbol{\sigma}$ is the stress tensor.

The starting point of the proposed model is a separation between damage and plasticity. The free energy is defined under the hypothesis of decoupling between elasticity-damage and plasticity and it is assumed that plasticity only evolves in the intact material and not in regions where the damage is activated. Thus, the specific free energy ψ is assumed to be split up into elastic-damage ψ^{ed} and plastic ψ^{p} contributions according to:

$$\psi(\boldsymbol{\varepsilon}^{\mathrm{e}}, d, \varepsilon_{\mathrm{eq}}^{\mathrm{p}}) = \psi^{\mathrm{ed}}(\boldsymbol{\varepsilon}^{\mathrm{e}}, d) + \psi^{\mathrm{p}}(\varepsilon_{\mathrm{eq}}^{\mathrm{p}}) \tag{3}$$

where $\varepsilon_{\mathrm{eq}}^{\mathrm{p}}$ and d are the internal variables, signifying the equivalent plastic strain and the damage, respectively.

For instance, assuming an elastic-damage potential that accounts for isotropic stiffness degradation gives:

$$\psi^{\mathrm{ed}}(\boldsymbol{\varepsilon}^{\mathrm{e}}, d) = \frac{1}{2}(1-d)\,\boldsymbol{\varepsilon}^{\mathrm{e}} : \mathbf{D}^{\mathrm{e}} : \boldsymbol{\varepsilon}^{\mathrm{e}} \tag{4}$$

where $\mathbf{D}^{\mathrm{e}}$ is the elasticity tensor from Hooke's law. The stress-strain relation is obtained by differentiating the potential as:

$$\boldsymbol{\sigma} = \frac{\partial \psi^{\mathrm{ed}}}{\partial \boldsymbol{\varepsilon}^{\mathrm{e}}} = (1-d)\,\mathbf{D}^{\mathrm{e}} : \boldsymbol{\varepsilon}^{\mathrm{e}} \tag{5}$$

The local energy release rate Y is defined as:

$$Y = -\frac{\partial \psi^{\mathrm{ed}}}{\partial d} = \frac{1}{2}\,\boldsymbol{\varepsilon}^{\mathrm{e}} : \mathbf{D}^{\mathrm{e}} : \boldsymbol{\varepsilon}^{\mathrm{e}} \tag{6}$$

Along with the loading/unloading conditions in Kuhn-Tucker form for time-independent models, Y is used to described the the damage evolution:

$$(Y - Y_c) \leq 0, \quad \dot{d} \geq 0, \quad \dot{d}(Y - Y_c) = 0 \tag{7}$$

in which Y_c is the material resistance to damage growth.

Using the effective stress concept, Eq. (5) can alternatively be expressed as:

$$\boldsymbol{\sigma} = (1-d)\,\hat{\boldsymbol{\sigma}} \tag{8}$$

where $\hat{\boldsymbol{\sigma}}$ is the effective stress defined as:

$$\hat{\boldsymbol{\sigma}} = \mathbf{D}^{\mathrm{e}} : \boldsymbol{\varepsilon}^{\mathrm{e}} = \mathbf{D}^{\mathrm{e}} : (\boldsymbol{\varepsilon} - \boldsymbol{\varepsilon}^{\mathrm{p}}) \tag{9}$$

In order to guarantee the admissibility of stresses, the yield criterion $f(\hat{\boldsymbol{\sigma}}, \varepsilon_{\mathrm{eq}}^{\mathrm{p}}) \leq 0$ must be satisfied. The plastic strain rate is written as the product of the plastic multiplier $\dot{\gamma}$ and the direction of plastic flow $\mathbf{n}$ [14]:

$$\dot{\boldsymbol{\varepsilon}}^{\mathrm{p}} = \dot{\gamma}\,\mathbf{n} \tag{10}$$

The evolution of plastic multiplier $\dot{\gamma}$ is such that the Kuhn-Tucker conditions are satisfied:

$$f \leq 0, \quad \dot{\gamma} \geq 0, \quad \dot{\gamma} f = 0 \tag{11}$$

The plasticity model is completed with an evolution law for the equivalent plastic strain, which is defined as a function of the equivalent plastic strain rate $\dot{\varepsilon}^{\mathrm{p}}_{\mathrm{eq}}$.

By design of the TLS, uncoupling damage from plasticity in terms of evolution of the internal variables can be achieved in a straightforward manner, since the level set field ϕ separates the domain Ω into an undamaged zone and a damaged one. In this case, the evolution of plasticity can only occur in zones where the level set function $\phi \leq 0$, whereas the TLS handles the damage evolution law in the region with $\phi > 0$ by taking the permanent strain contribution into account via Eq. (9). Therefore, the damage front decides where and when the plasticity is evaluated.

2.2. Plasticity model

In this section, the equations presented in Section 2.1 for a general plasticity model are particularized to the pressure-dependent plasticity model for polymers by Melro *et al.* [13] as adapted by Van der Meer [15]. The backward Euler scheme is considered to discretize all rate quantities for plasticity. Because plasticity is only updated where $d = 0$ and $\boldsymbol{\sigma} = \hat{\boldsymbol{\sigma}}$, the hat symbol on the effective stress tensor is dropped.

A paraboloidal yield surface is considered:

$$f(\boldsymbol{\sigma}, \varepsilon^{\mathrm{p}}_{\mathrm{eq}}) = 6J_2 + 2I_1(\sigma_c - \sigma_t) - 2\sigma_c\sigma_t \tag{12}$$

with

$$\sigma_c = \sigma_c(\varepsilon^{\mathrm{p}}_{\mathrm{eq}}) \quad \text{and} \quad \sigma_t = \sigma_t(\varepsilon^{\mathrm{p}}_{\mathrm{eq}}) \tag{13}$$

where J_2 is the second invariant of the deviatoric stress tensor, I_1 is the first invariant of the stress tensor, and σ_c and σ_t are the uniaxial compressive and tensile yield stresses, respectively. The pressure dependency comes from the term $2I_1(\sigma_c - \sigma_t)$. For the case of $\sigma_c = \sigma_t$, the yield surface is equivalent to the classic Von Mises criterion. Both σ_c and σ_t are defined as a function of $\varepsilon^{\mathrm{p}}_{\mathrm{eq}}$ to match measured hardening curves.

If the material is loaded at the yield stress, plastic flow takes place. Using a non-associative flow rule, the plastic strain increment (cf. Eq. (10)) is given by:

$$\Delta\boldsymbol{\varepsilon}^{\mathrm{p}} = \Delta\gamma\left(3\mathbf{S} + \frac{2}{9}\alpha I_1\mathbf{I}\right) \tag{14}$$

where $\mathbf{S}$ is the deviatoric stress tensor, $\mathbf{I}$ is the identity matrix, and α is the parameter that controls the plastic volumetric flow and depends on the plastic Poisson's ratio ν_p:

$$\alpha = \frac{9}{2}\frac{1-2\nu_p}{1+\nu_p} \tag{15}$$

The increment of the equivalent plastic strain $\varepsilon^{\mathrm{p}}_{\mathrm{eq}}$ is defined as:

$$\Delta\varepsilon^{\mathrm{p}}_{\mathrm{eq}} = \sqrt{k\Delta\boldsymbol{\varepsilon}^{\mathrm{p}} : \Delta\boldsymbol{\varepsilon}^{\mathrm{p}}} \tag{16}$$

in which $k = 1/(1+2\nu_p^2)$.

In order to check for admissibility of stress state and determine the increment of the plastic multiplier $\Delta\gamma$ such that the constraints in Eq. (11) are satisfied, an iterative elastic predictor/return mapping algorithm is used. Details on the return mapping algorithm and the consistent tangent matrix can be found in [15].

2.3. Thick Level Set method

In the TLS, the front of one or more damaged zones is implicitly represented as the isocontour (or level set) of an auxiliary field and its evolution is accomplished by the level set method [3, 4]. The advantage of the level set method is that one can deal with geometric features (e.g. merging and branching) involving surfaces or curves on a discretized domain, without having to explicitly mesh boundaries of these objects. The location of the front Γ_0 is tracked as the zero level set (or iso-zero) of a single auxiliary field $\phi(\mathbf{x})$ (see Fig. 1).

If ϕ is a smooth well-behaved function, the definition of ϕ on a discretized domain at a given point $\mathbf{x}$ is determined by interpolating the values of ϕ from nodes to $\mathbf{x}$. A convenient choice for definition of ϕ is the signed distance function [3, 4], which is mathematically equivalent to:

$$|\nabla\phi| = 1 \quad \text{on} \quad \Omega \tag{17}$$

By definition, this choice for ϕ guarantees that the absolute value of ϕ at a given point is the shortest distance to the front from that point.

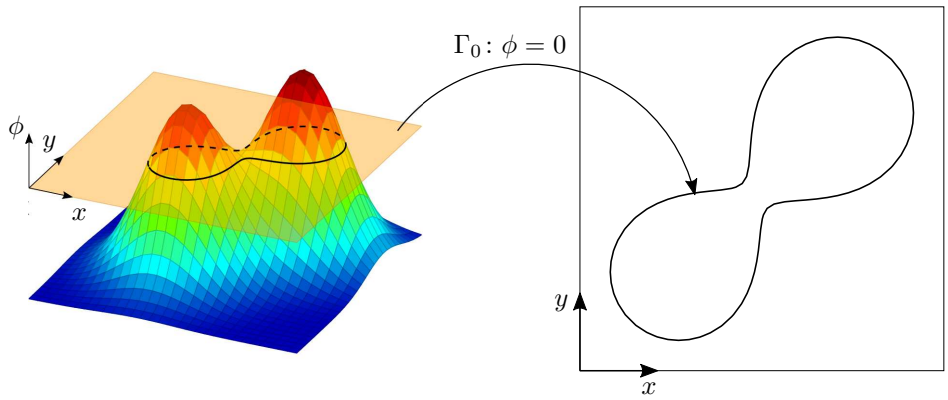

Figure 1: The level set method: the front Γ_0 is implicitly located as the zero level set of ϕ.

2.3.1. Damage definition

As it has been mentioned, the level set $\phi = 0$ separates the domain Ω into an undamaged zone and a damaged one, and ϕ is known at every point. In the TLS, the damage variable d is chosen to depend only on ϕ. As depicted in Fig. 2, d is assumed to change from zero to one as ϕ goes from zero to the critical length l_c. Mathematically, the damage variable is expressed by:

$$d(\phi) = \begin{cases} 0, & \phi \leq 0 \\ q(\phi), & 0 < \phi \leq l_c \\ 1, & \phi > l_c \end{cases} \tag{18}$$

where q is a function that has the properties of $q(0) = 0$, $q(l_c) = 1$ and $q' \geq 0$.

An arc-tangent formula is used for $q(\phi)$:

$$q(\phi) = c_2 \arctan\left(c_1 \left(\frac{\phi}{l_c} - c_3\right)\right) + c_4 \tag{19}$$

Following Bernard *et al.* [2] and Van der Meer and Sluys [5], all computations are performed with $c_1 = 10$ and $c_3 = 0.5$, which lead to a point symmetric profile as schematically represented in Fig. 2. The other constants c_2 and c_4 are determined to satisfy the conditions $q(l_c) = 1$ and $q(0) = 0$, respectively:

$$c_2 = \left(\arctan\left(c_1 \left(1 - c_3\right)\right) - \arctan\left(-c_1 c_3\right)\right)^{-1} \tag{20}$$

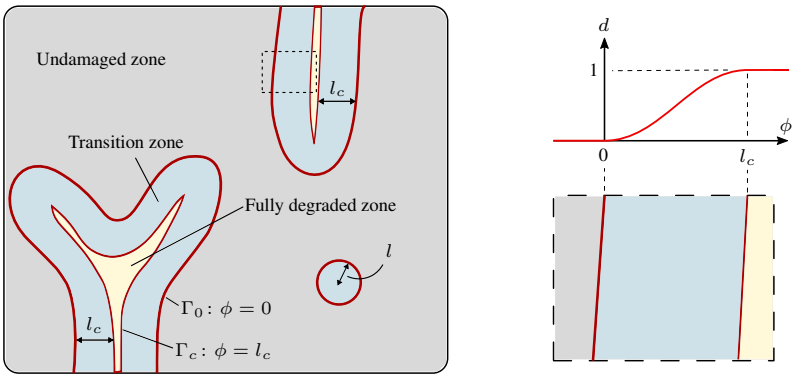

Figure 2: The TLS makes use of a single level set function to describe multiple zones. As illustrated on the right, the damage variable d is a function of level set ϕ.

$$c_4 = -c_2 \arctan\left(-c_1 c_3\right) \tag{21}$$

The position of the macro-cracks is located in the zone at a distance larger than l_c behind the front where $d = 1$. This region is easily identified due to the fact that ϕ is a distance function. To accommodate localized deformations, the elements crossed by the iso-l_c of the level set field need some particular enrichment in order to introduce a discontinuity in strain and provide strain-free localization at crack lips, as explained in [2].

2.3.2. Free energy: asymmetric behavior in tension/compression

The free energy expression in Eq. (4) leads to material laws that present the same behavior in tension and compression, which can be applicable to failure analysis in tension dominated cases. However, if the damaged zone experiences compression, the energy release rate Y in Eq. (6) would still be nonzero, which may result in unphysical compressive cracks. For simulation of cases subjected to shear load conditions, this formulation leads to unrealistic 'X-shaped' cracks as reported by Van der Meer and Sluys [5].

Therefore, the free energy density expression from [2, 5] that accounts for stiffness recovery under compression is used in this paper:

$$\psi^{\mathrm{ed}}(\boldsymbol{\varepsilon}^{\mathrm{e}}, d) = \mu(1 - \alpha_i d)(\varepsilon_i^{\mathrm{e}})^2 + \frac{\lambda}{2}(1 - \alpha_v d)\mathrm{tr}(\boldsymbol{\varepsilon}^{\mathrm{e}})^2 \tag{22}$$

where λ and μ are the Lamé's elastic constants, $\varepsilon_i^{\mathrm{e}}$ the eigenvalues of the elastic strain tensor, and the α_i and α_v parameters relate the activation of

damage to the principal strain $\varepsilon_i^{\mathrm{e}}$ and the volumetric strain $\varepsilon_v = \mathrm{tr}(\boldsymbol{\varepsilon}^{\mathrm{e}})$, respectively. Each of these constants assumes the value of 1 or 0 depending on the sign of the associated strain quantity in such way that if one of the principal strains or the volumetric strain becomes negative, the stiffness degradation is canceled for the corresponding term:

$$\alpha_i = \begin{cases} 1, & \varepsilon_i^{\mathrm{e}} > 0 \\ 0, & \varepsilon_i^{\mathrm{e}} < 0 \end{cases} \quad \text{and} \quad \alpha_v = \begin{cases} 1, & \mathrm{tr}(\boldsymbol{\varepsilon}^{\mathrm{e}}) > 0 \\ 0, & \mathrm{tr}(\boldsymbol{\varepsilon}^{\mathrm{e}}) < 0 \end{cases} \tag{23}$$

By the definitions in Eqs. (5) and (6), the stress-strain relation and the driving force for damage growth can be rewritten as follows:

$$\sigma_i = \frac{\partial \psi^{\mathrm{ed}}}{\partial \boldsymbol{\varepsilon}^{\mathrm{e}}} = 2\mu(1 - \alpha_i d)\varepsilon_i^{\mathrm{e}} + \lambda(1 - \alpha_v d)\mathrm{tr}(\boldsymbol{\varepsilon}^{\mathrm{e}}) \tag{24}$$

and

$$Y = -\frac{\partial \psi^{\mathrm{ed}}}{\partial d} = -\mu\alpha_i(\varepsilon_i^{\mathrm{e}})^2 - \frac{\lambda}{2}\alpha_v \mathrm{tr}(\boldsymbol{\varepsilon}^{\mathrm{e}})^2 \tag{25}$$

One can observe, the damage has no effect on the material in compression: the undamaged stiffness is recovered and Y becomes zero, which means damage does not grow.

2.3.3. Non-local evolution law

In the TLS approach, the non-locality is evident when the front moves [2]. Because the updating of the signed distance function, all points sharing the same curvilinear coordinate s[1] are affected as the front at $(0, s)$ moves (see Fig. 3). Therefore, the amount of energy per unit length that will be dissipated as the front moves a unit distance reads:

$$g(s) = \int_0^l d'(\phi) Y(\phi, s) \left(1 - \frac{\phi}{\rho(s)}\right) \mathrm{d}\phi \tag{26}$$

where $d'(\phi) = q'(\phi)$ is the spatial derivative of damage with respect to ϕ, l is the size of the damaged zone $l \in (0, l_c]$ (see Fig. 2) and ρ is the curvature of iso-zero.

[1] A curvilinear system of coordinates (ϕ, s) using the change of variable $\mathrm{d}\Omega = \left(1 - \frac{\phi}{\rho(s)}\right) \mathrm{d}\phi \mathrm{d}s$ is introduced for derivation, following Moës *et al.* [1]. In the implementation, the curvilinear coordinate system does not need to be defined.

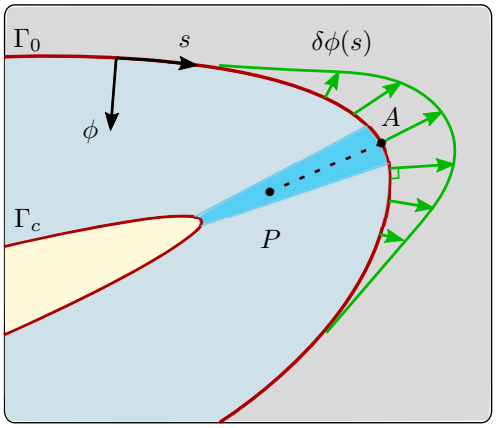

Figure 3: Curvilinear coordinate system (ϕ, s). Point P is affected as point A on the front experiences a front advance.

Now, the loading/unloading condition in Eq. (7) can be rewritten in terms of non-local energy release rate $g(s)$ and $g_c(s)$. However, for nucleation, that is, in the limit case that l tends to 0, $g(s)$ vanishes. Hence, in order to be able to capture nucleation and smaller damaged zones, the averaged value of Y across the damaged band is introduced as proposed by Bernard *et al.* [2]. For any position along the front, the averaged value $\bar{Y}$ is defined as the value that satisfies:

$$\int_0^l d'(\phi) Y(\phi, s) \left(1 - \frac{\phi}{\rho(s)}\right) \mathrm{d}\phi = \int_0^l d'(\phi) \bar{Y}(s) \left(1 - \frac{\phi}{\rho(s)}\right) \mathrm{d}\phi \tag{27}$$

The averaged configuration force $\bar{Y}$, which tends to Y as l tends to zero, is thus a weighted average of Y. Finally, the front velocity v_n is defined as a function of $\bar{Y}$ and $\bar{Y}_c$, the weighted average of Y_c (see Subsection 2.3.4).

In order to compute the averaged configurational force along the front and avoid direct computation of the term depending on the curvature ρ, Eq. (27) is discretized as a field on the damaged domain Ω^d with $\bar{Y}$ as unknown. Following Bernard *et al.* [2], the constraint that $\bar{Y}$ must be constant along the level set gradient, i.e. $\nabla\bar{Y} \cdot \nabla\phi = 0$, is enforced with Lagrange multipliers. A discretized approximation of $\bar{Y}$ is introduced in combination with Galerkin's method leading to the following system of equations:

$$\begin{bmatrix} \mathbf{K} & \mathbf{L} \\ \mathbf{L} & \mathbf{0} \end{bmatrix} \begin{Bmatrix} \bar{\mathbf{Y}} \\ \mathbf{l} \end{Bmatrix} = \begin{Bmatrix} \mathbf{f}^{\mathrm{Y}} \\ \mathbf{0} \end{Bmatrix} \tag{28}$$

in which $\bar{\mathbf{Y}}$ and $\mathbf{l}$ are vectors with $\bar{Y}$ and Lagrange multiplier degrees of freedom, respectively. The matrices and the right-hand side vector are defined as:

$$K_{ij} = \int_{\Omega^d} d' N_i N_j + \frac{\kappa h^2}{l_c} \frac{\partial N_i}{\partial x_k} \frac{\partial N_j}{\partial x_k} \mathrm{d}\Omega \tag{29}$$

$$L_{ij} = \int_{\Omega^d} l_c \left(\frac{\partial N_i}{\partial x_k} \frac{\partial \phi}{\partial x_k} \right) \left(\frac{\partial N_j}{\partial x_k} \frac{\partial \phi}{\partial x_k} \right) \mathrm{d}\Omega \tag{30}$$

$$f_i^{\mathrm{Y}} = \int_{\Omega^d} N_i d' Y \mathrm{d}\Omega \tag{31}$$

where N_i and N_j are the shape functions associated with nodes i and j, κ is a stabilization parameter, h is the characteristic size of the smallest element, and Y is the configurational force which depends on the current elastic strain field evaluated through Eq. (25). If the damage resistance Y_c is not constant over the domain, a similar system of equations, with a different right hand side where Y_c is used instead of Y, is solved to compute $\bar{Y}_c$.

2.3.4. Front movement

To update the damage distribution, the advance of the level set field should be related to the configurational force $\bar{Y}$ and material resistance against damage growth $\bar{Y}_c$. The change in the level set field is related to the normal velocity of the front as:

$$\frac{\partial \phi}{\partial t} + v_n |\nabla \phi| = 0 \tag{32}$$

In absence of physical time in quasi-static simulations, the TLS does not directly work with velocities but with a front increment. In this case, $v_n \Delta t$ is regarded as the front increment. Using forward Euler time discretization and the property of $|\nabla \phi| = 1$, the update of the level set field is performed as:

$$\phi \leftarrow \phi + v_n \Delta t \tag{33}$$

where Δt is the time increment size.

In the previous version of the TLS [1, 2, 5], the loading scheme was based on a unit load analysis in each time step, computing a critical load scale factor under the assumption of secant unloading. This loading scheme is not

applicable when permanent strain due to plasticity is considered. Therefore, the framework of TLS must be adapted. Here, the following relation for the normal velocity is used, given by [16, 17]:

$$v_n = \frac{1}{\eta}\left\langle \frac{\bar{Y}}{\bar{Y}_c} - 1 \right\rangle_+ \tag{34}$$

where η is a parameter that can be interpreted as viscous resistance against crack growth. In the limit of $\eta \to 0$, the Kuhn-Tucker conditions for quasi-static crack growth with $\bar{Y} - \bar{Y}_c \leq 0$ are approached. Brackets are used to denote the positivity condition, which reflects the irreversibility of crack growth.

In order to ensure stability of the explicit level set update, the Courant-Friedrichs-Lewy condition is applied [4]:

$$\Delta t < \frac{h}{\max\{v_n\}} \tag{35}$$

where h is the characteristic size of the smallest element and $\max\{v_n\}$ is the largest value of v_n over the entire domain. Here, this conditions is rewritten in a more conservative form according to [4, 16]:

$$\Delta t = \min\left\{ \Delta t^0,\ \alpha_n \frac{h}{\max\{v_n\}} \right\} \tag{36}$$

in which Δt^0 is the default and maximum time increment and α_n is a constant defined as $0 < \alpha_n < 1$.

The level set update with Eq. (33) requires the velocity to be known throughout the domain. However, Eq. (34) is only calculated along the front. The velocity computed at the nodes of elements that contain the front is propagated through the domain by solving:

$$\nabla\phi \cdot \nabla v_n = 0 \tag{37}$$

This is done with a fast marching method [3, 4, 16]. When the level set field ϕ^n in the previous time step n, which is a signed distance function, moves $v_n \Delta t$ units forward in the normal direction, the updated level set field ϕ^{n+1} obtained by Eq. (33) remains a signed distance function. This arises from the fact that the gradient of Eq. (33) leads to $\nabla\phi^{n+1} = \nabla\phi^n$, since $v_n \Delta t$ is

spatially constant in ϕ direction, i.e. $\nabla_\phi(v_n \Delta t) = 0$. Thus, if ϕ^n is initially a signed distance function, it will stay a signed distance function [3, 4].

However, in the discretized model, the level set field may drift away from being an accurate representation of signed distance. Thus, another fast marching method needs to be applied periodically in order to keep ϕ as signed distance function [16]. Since it is a relatively cheap procedure, this reinitialization is performed every time step.

2.3.5. Initiation

To deal with damage activation for the proposed model, the criterion $Y \geq Y_c$ must be satisfied at undamaged point. Note that this criterion is purely local, which is consistent with Eq. (27), since $\bar{Y}$ and $\bar{Y}_c$ tend to Y and Y_c as l tends to zero. When this criterion is met at any point, a circle with radius $\phi_0 < l_c$ is inserted around that point and the signed distance function is reinitialized accordingly. The size of this nucleus from then on increases according to the same framework as introduced in Subsections 2.3.3 and 2.3.4.

Following the proposed model in [5], the resistance Y_c is made into a function of the size of the damaged zone in order to handle initiation and propagation with separate material parameters. In this approach, Y_c changes from an initial strength-based value for initiation Y_c^0 to a fracture energy-based value for crack growth Y_c^G, as the size of the damaged zone changes from zero to a circle with radius l_c. The intermediate values of Y_c are interpolated between the two bounds in the space of $\log(Y_c)$:

$$\log(Y_c) = \log(Y_c^0) + \frac{\bar{\phi}}{\bar{\phi}_{\max}} \left(\log(Y_c^G) - \log(Y_c^0) \right) \tag{38}$$

where $\bar{\phi}$ is a measure for the size of a damaged zone over a closed damaged subdomain defined as the average of ϕ over the subdomain and $\bar{\phi}_{\max}$ represents the size for which the damaged zone is considered a crack. In Fig. 4, three stages are schematically sketched as $\bar{\phi}$ varies from $\bar{\phi} = 0$, for a very small circle with radius ϕ_0, to $\bar{\phi} = \bar{\phi}_{\max}$, for a circle with radius l_c, to $\bar{\phi} = l_c/2$, for a long straight damaged zone with width $2l_c$.

The averaged value $\bar{\phi}$ is computed in each time step in a similar way as $\bar{Y}$ in Eq. (28) by substituting level set values ϕ and unknowns $\bar{\phi}$ for Y and $\bar{Y}$, respectively, and omitting the weight factor d' from left-hand side matrix and right-hand side vector. Variation of $\bar{\phi}$ in the normal direction is

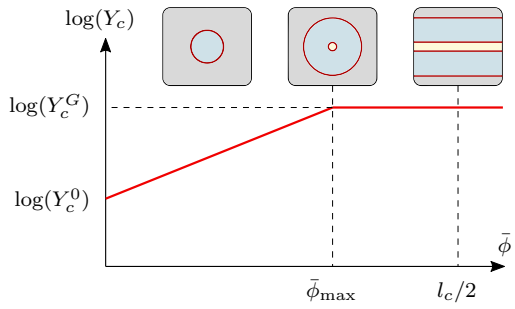

Figure 4: Interpolation of Y_c between Y_c^0 and Y_c^G (adapted from [5]).

again eliminated with Lagrange multipliers, while variation in the curvilinear direction is eliminated by considering a high value for κ [5].

In contrast to what was proposed in [5], in which Y_c^0 was set to a constant value equal to the free energy in the case where the uniaxial stress equals the tensile strength, Y_c^0 is here bounded by the following surface based on Eq. (12):

$$f^0 = \frac{3\hat{J}_2}{f_c f_t} + \frac{\hat{I}_1\,(f_c - f_t)}{f_c f_t} - 1 = 0 \tag{39}$$

with f_c and f_t being the compressive and the tensile strengths which are set equal to the ultimate yield stress values of the material. The two invariants $\hat{J}_2$ and $\hat{I}_1$ are determined using the effective stress. The motivation to use such surface for Y_c^0 comes from the fact that Y_c^0 as a function of a single parameter f_t may prohibit initiation for certain stress states when a plasticity model with perfectly plastic tail is used. For the particular case where a uniaxial tensile strength equals f_t, a constant Y_c^0 would be defined as (see Eq. (25)):

$$Y_c^0(f_t) = \frac{f_t^2}{2E}\left(\frac{1 + 2\nu - 2\nu^2}{1+\nu}\right) \tag{40}$$

where E is the Young's modulus and ν is the Poisson's ratio. Note that the term depending on ν in the expression above is a correction factor which was missing in the previous TLS model (cf. [5], where $Y_c^0 = f_t^2/2E$). This factor is needed because under uniaxial tension not all α's in Eq. (22) evaluate to 1.

Fig. 5 illustrates the problem of using the constant $Y_c^0(f_t)$ from Eq. (40) as initiation criterion in presence of plasticity with a given ultimate yield surface f^0 that bounds the admissible stress states. It can be observed

that, if the ultimate uniaxial tensile yield stress is used for f_t in $Y_c^0(f_t)$, no initiation under pure shear is possible. The damage cannot be activated since the plasticity bounds the stress states.

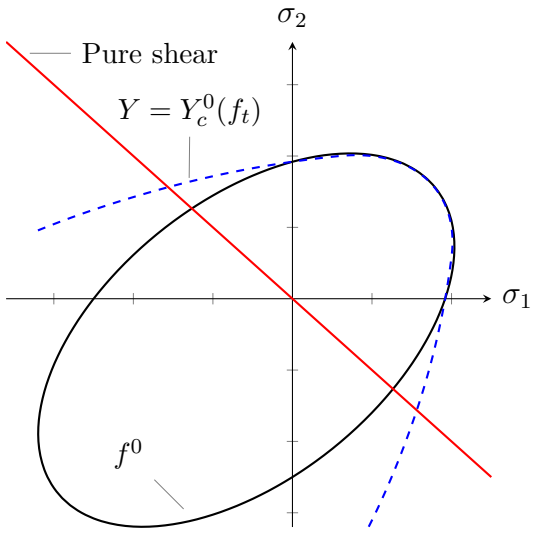

Figure 5: Envelopes in principal stress space illustrating the inability of the criterion $Y = Y_c^0(f_t)$, related to the single parameter f_t, to deal with damage initiation under pure shear.

This illustrates that, in presence of plasticity, more control is needed over the initiation envelope. Here, a relation is devised between Y_c^0 and the stress orientation so that the failure envelope coincides with the final yield surface given by f^0. The relation for Y_c^0 is for 2D plane stress state derived as a function of the angle θ, defined in principal stress space as $\theta = \arctan(\sigma_2/\sigma_1)$. The idea is that for a given stress vector $\boldsymbol{\sigma}(\sigma_1,\sigma_2)$, Y_c^0 is given as $Y_c^0(\boldsymbol{\sigma}_c^0)$, with the critical stress vector $\boldsymbol{\sigma}_c^0(\sigma_{c1}^0, \sigma_{c2}^0)$ on f^0 obtained by scaling $\boldsymbol{\sigma}$ through:

$$\boldsymbol{\sigma}_c^0 = \frac{r}{|\boldsymbol{\sigma}|}\boldsymbol{\sigma} \tag{41}$$

where r corresponds to the norm $|\boldsymbol{\sigma}_c^0|$, as illustrated in Fig. 6. To evaluate r as a function of $\boldsymbol{\sigma}$, the length of the 'radius' r is parametrically written as an ellipse with a single parameter θ.

The parametric equation for r as a standard form of an ellipse can be deduced from the fact that Eq. (39) under plane stress assumption can be

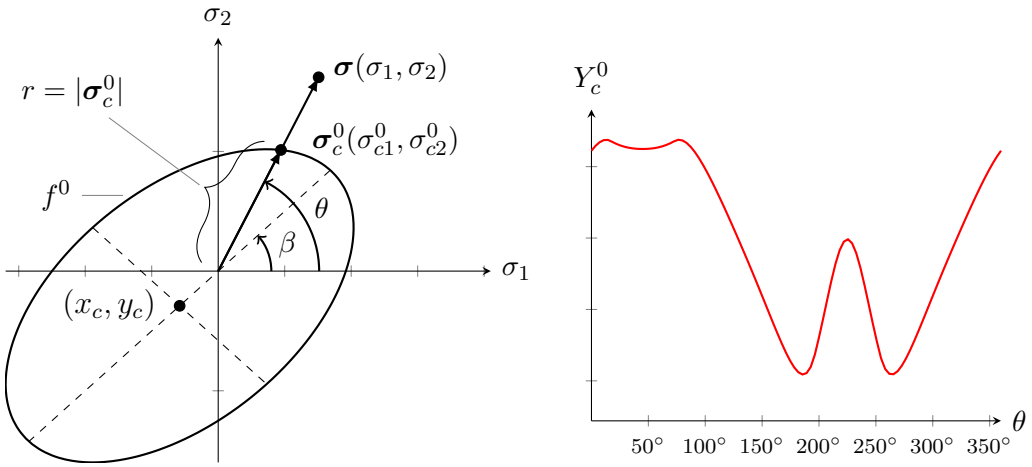

Figure 6: Definition of the length of r (left) and resulting Y_c^0 as a function of θ.

rewritten in principal stress space as:

$$f^0 = A\sigma_1^2 + B\sigma_1\sigma_2 + C\sigma_2^2 + D\sigma_1 + E\sigma_2 + F = 0 \tag{42}$$

with $A = C = \frac{1}{f_c f_t}$, $B = -\frac{1}{f_c f_t}$, $D = E = \frac{(f_c - f_t)}{f_c f_t}$ and $F = -1$. The discriminant of the equation above, which is defined as $\Delta = B^2 - 4AC$, is always negative, which implies that Eq. (42) represents an ellipse [18, 19]. In this case, Eq. (42) can be written as the standard expression for an ellipse centered at (x_c,y_c) and rotated through an angle β (see Fig. 6):

$$\frac{x^2}{a^2} + \frac{y^2}{b^2} = 1 \tag{43}$$

where

$$\begin{aligned} x &= (\sigma_1 - x_c)\cos\beta + (\sigma_2 - y_c)\sin\beta \\ y &= -(\sigma_1 - x_c)\sin\beta + (\sigma_2 - y_c)\cos\beta \end{aligned} \tag{44}$$

in which x_c, y_c, β, and the axes of the ellipse a and b are expressed as a function of the constants A, B, C, D, E and F [18, 19]. For this particular case, one can show that $\beta = 45°$ and $x_c = y_c = D/B$. Substitution of the relations $\sigma_1 = r\cos\theta$ and $\sigma_2 = r\sin\theta$ into Eq. (44) and Eq. (43) leads to a quadratic equation, which is solved for r, where the positive root is chosen. Note that such approach can also directly be performed in principal strain space by expressing $\hat{J}_2$ and $\hat{I}_1$ as a function of principal strains and Lamé's elastic constants which could allow for generalization to 3D.

The remaining parameter Y_c^G is computed from the fracture energy G_c and l_c by considering the following relation [2]:

$$G_c = 2AY_c^G l_c \tag{45}$$

with A the area under the curve d. For the point symmetric damage profile, $A = 0.5$.

2.4. Mapping operators

In the TLS, integration points, from one load increment to another, are dynamically allocated for elements that are cut by iso-0 and iso-l_c, in order to improve the accuracy of numerical integration. This is not an issue for elastic materials if one uses a total stress-strain formulation. On the other hand, in the case of crack propagation in elastic-plastic materials, history terms influence the local response. These history terms are stored at integration points. When the integration scheme changes, transfer of history terms from 'old' to 'new' integration points is needed. In this study, the inverse distance weighted interpolation [20] and the superconvergent patch recovery (SPR) [21, 22, 23] techniques for transferring plasticity terms between old and new integration schemes are compared. For the elasto-plastic model, the plastic strain tensor $\boldsymbol{\varepsilon}^{\mathrm{p}}$ and the equivalent plastic strain $\varepsilon_{\mathrm{eq}}^{\mathrm{p}}$ are the history variables that need to be transferred.

2.4.1. Inverse distance weighted interpolation

Let s_i^{old} be an old history term at an old integration point i. With inverse distance-based interpolation, the new history term s_j^{new} at a new integration point j is given by:

$$s_j^{\mathrm{new}} = \frac{\sum_{i=1}^{n_{\mathrm{old}}} s_i^{\mathrm{old}} \left(1/l_{ij}\right)}{\sum_{i=1}^{n_{\mathrm{old}}} \left(1/l_{ij}\right)} \tag{46}$$

where n_{old} is the number of old integration points in an element and l_{ij} is the distance between an old integration point i and a new integration point j inside the same element (see Fig. 7). If a new integration point coincides with an old one, the old history is kept.

2.4.2. Superconvergent patch recovery

The SPR technique is carried out in two steps. Firstly, a history term s_k^N at a node k within an element patch (see Fig. 8) is estimated by:

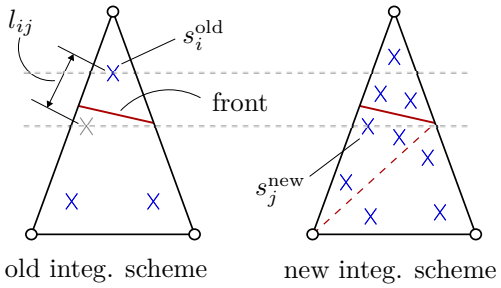

Figure 7: Inverse distance weighted interpolation: sub-triangulation.

$$s_k^N = \mathbf{P}\mathbf{a} \tag{47}$$

where $\mathbf{P}$ contains the appropriate terms of a complete polynomial expansion of order p and $\mathbf{a}$ is a set of unknown coefficients. For two dimensions and quadratic expansion, for instance:

$$\mathbf{P}(x, y) = \begin{bmatrix} 1 & x & y & x^2 & xy & y^2 \end{bmatrix} \tag{48}$$

and

$$\mathbf{a} = \begin{bmatrix} a_1 & a_2 & a_3 & a_4 & a_5 & a_6 \end{bmatrix}^{\mathrm{T}} \tag{49}$$

The coefficients in $\mathbf{a}$ are determined via the least square method fitting from the integration points within the element patch, which results in:

$$\mathbf{a} = \mathbf{A}^{-1}\mathbf{b} \tag{50}$$

where

$$\mathbf{A} = \sum_{i=1}^{n_p} \mathbf{P}(x_i, y_i)^{\mathrm{T}} \mathbf{P}(x_i, y_i) \tag{51}$$

and

$$\mathbf{b} = \sum_{i=1}^{n_p} \mathbf{P}(x_i, y_i)^{\mathrm{T}} s_i^{\text{old}} \tag{52}$$

with n_p and (x_i, y_i) being the total number and coordinates of integration points in the element patch, respectively. Secondly, the new history terms at a new integration point j are obtained by shape function interpolation, which has the same order p as $\mathbf{P}$:

$$s_j^{\text{new}} = \mathbf{N}\mathbf{s}^N \tag{53}$$

It must be emphasized that Eq. (50) is evaluated for each history term using the same matrix solution. Besides, only a single evaluation of $\mathbf{A}$ is necessary per patch. Once $\mathbf{a}$ is determined, the recovery nodal values s^N are simply computed by inserting the appropriate coordinates into Eq. (47). In Fig. 8, for instance, the nodes for linear and quadratic triangular elements that are considered for recovery are shown. For internal element nodes ($p \geq 2$), which cannot be an assembly node, the history terms will be considered from several patches and they are therefore averaged as suggested in [21, 22, 23]. For nodes at boundaries and nodes that give rise to a patch with a single element, such nodes cannot be an assembly node and they are recovered as an internal element node [21, 22].

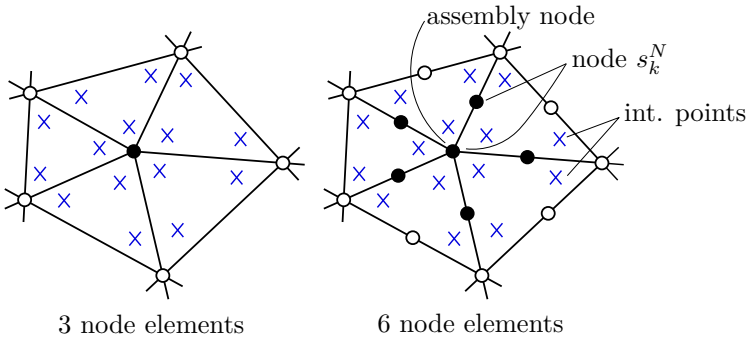

Figure 8: Triangular element patches for linear and quadratic finite elements: • nodal values determined by recovery procedure (Eq. (47)).

2.4.3. Verification: 1D problem

A 1D model is developed (see Fig. 9) to assess the performance of both operators for plasticity quantities and answer the question which the most suitable for the TLS with a moving front and frozen history behind the front. In this simulation, a uniform mesh of linear truss elements with two nodes, uniform cross-section area and two integration point are used. When an element is cut by the front, two more integration points are added to that element. An elementary constitutive model for linear isotropic hardening plasticity is used as presented in [24] and shown in Fig. 9. The expressions needed to implement the elastic predictor/return mapping algorithm

and tangent modulus D for this model can also be found in a closed-form analytical manner in [24].

The bar is constantly loaded with rate $\dot{u}^0 = \Delta u^0/\Delta t^0 = 0.01\,\mathrm{mm\,s^{-1}}$. Young's modulus, hardening modulus, length and cross-section area are, respectively, $E = 200\,\mathrm{GPa}$, $K = 5\,\mathrm{GPa}$, $L = 1.5\,\mathrm{m}$ and $A = 100\,\mathrm{mm^2}$. When the uniaxial stress reaches immediately around the yield stress $\sigma_y = 250\,\mathrm{MPa}$, the front l starts to move from left to right side. From this stress level, the front moves continuously with a constant velocity $v_n = 0.02\,\mathrm{mm\,s^{-1}}$ from $l = 0.55\,\mathrm{m}$ to $l = 1\,\mathrm{m}$. In line with the proposed TLS framework, the plasticity is not allowed to increase behind the front.

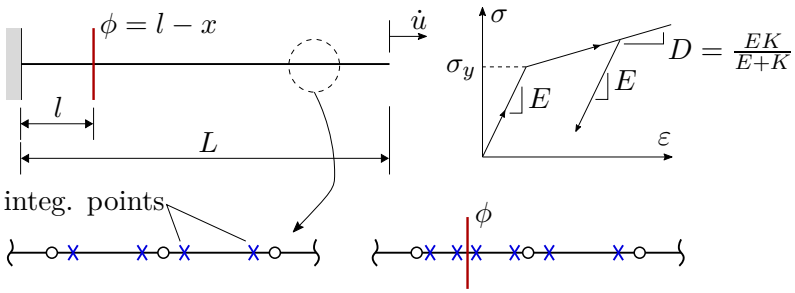

Figure 9: 1D problem for assessing the performance of mapping operators. The level set value ϕ at coordinate x is related to the position of the front l.

A reference response is also computed with a mesh of 500 elements. For this response, each finite element has 100 integration points and the integration scheme does not change. In Fig. 10, a comparison between results obtained with the two operators and the reference response is shown in terms of a load-displacement curve, obtained with a mesh with three elements for both operators, along with a convergence study. For the convergence study, the areas under load-displacement graphs are used and their relative differences are computed between the two operators and the reference response. It is clear particularly for coarse meshes that the SPR technique performs better than inverse distance-based interpolation as reported in both graphs in Fig. 10. Therefore, for sake of robustness and accuracy, the SPR technique is used for all the numerical examples presented in this paper.

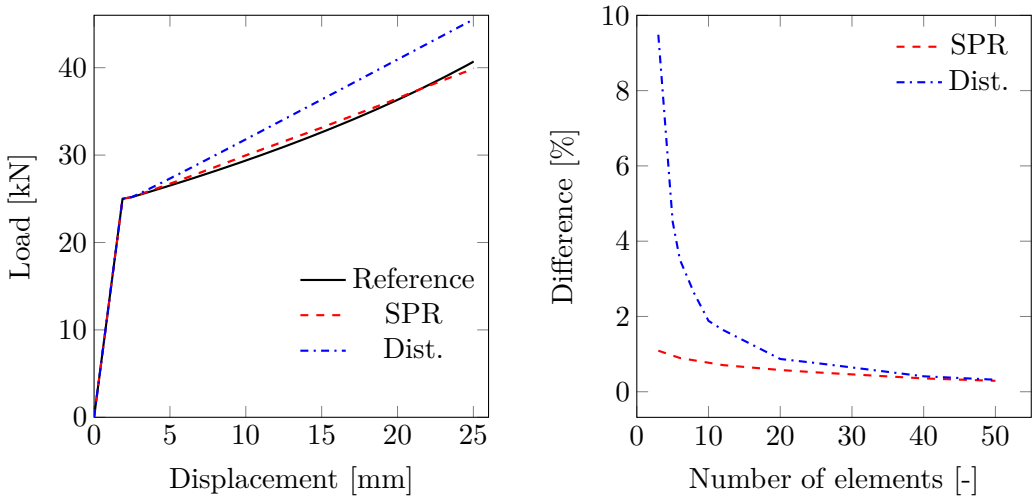

Figure 10: Typical load-displacement graph and convergence study for 1D problem.

2.5. Algorithm

In Box 1, the global algorithm solution, where the problem is solved in a staggered fashion [2, 5], is schematically summarized. Every time step consists of three main parts. Firstly, damage initiation is evaluated, ϕ is reinitialized in order to guarantee the properties of a signed distance function and $\bar{\phi}$ is computed. Secondly, with a given damage distribution, the displacements, and consequently strains and stresses are computed according to a standard finite element analysis for elasto-plastic constitutive models in conjunction with the concept of effective stress. The plastic state is only updated for integration points in undamaged zones. Finally, the displacements, permanent strains and $\bar{\phi}$ are used to compute the configurational force $\bar{Y}$ and the material resistance $\bar{Y}_c$. In this part, the velocities are first computed at nodes of elements that contain the front and subsequently extended by a fast marching method. Before going to the next time step, the time increment size is adjusted based on the stability condition if necessary.

The update of prescribed displacement for the following time step is performed according to the same adaptive time step size:

$$u \leftarrow u + \Delta u^0 \frac{\Delta t}{\Delta t^0} \tag{54}$$

This allows to capture sharp load drops. If $\bar{Y}$ becomes very high, Δt will become very small, which results in a restraint on the increase in prescribed displacement during unstable damage growth.

For each time step:

1. Damage distribution:
   (a) Add new front ϕ_0 for nucleation if $Y \geq Y_c$ is met
   (b) Reinitialize ϕ on the whole domain with fast marching method (optionally only every n steps)
   (c) Assemble and solve linear system similar to Eq. (28) for $\bar{\phi}$
2. Finite element analysis:
   (a) Update of prescribed displacements (Eq. (54))
   (b) Compute displacements, strains and stresses. Plastic state is only evaluated for integration points in undamaged zone
3. Grow fronts:
   (a) Compute configurational force $\bar{Y}$ and material resistance $\bar{Y}_c$ (Eqs. (28) and (38))
   (b) For nodes on fronts, compute normal velocity v_n (Eq. (34))
   (c) Extend normal velocity over the entire domain: solving $\nabla\phi \cdot \nabla v_n = 0$ (Eq. (37)) with fast marching method
   (d) Adjust new time increment size Δt (Eq. (36))
   (e) Update level set field: $\phi \leftarrow \phi + v_n \Delta t$ (Eq. (33))

Box 1: Global algorithm for single time step.

3. Results and discussion

The numerical examples in this section are performed with $\kappa = 1$ for $\bar{Y}$ (Eq. (28)) and $\kappa = 1 \cdot 10^4$ for $\bar{\phi}$. For nucleation, the size of a new damage nucleus is set to $\phi_0 = 0.1 l_c$. Furthermore, the constant α_n in Eq. (36) is set to $\alpha_n = 0.5$, $\bar{\phi}_{\max} = l_c/3$ [5] and the default displacement rate is $\dot{u}^0 = \Delta u^0 / \Delta t^0 = 0.005\,\mathrm{mm\,s^{-1}}$. The obtained results are quantitatively and qualitatively compared with those available in the literature. Unstructured meshes of triangles generated with Gmsh [25] are used.

3.1. V-notched bar

In this section, the plane strain response of a V-notched specimen in tension is investigated. The aim of this example is to demonstrate the ability of the proposed model to deal with ductile fracture by means of comparisons against experimental data by Li *et al.* [26] and numerical results by Miehe *et*

al. [27]. Boundary conditions and geometry of the V-notched specimen are demonstrated in Fig. 11. The model properties are listed in Table 1.

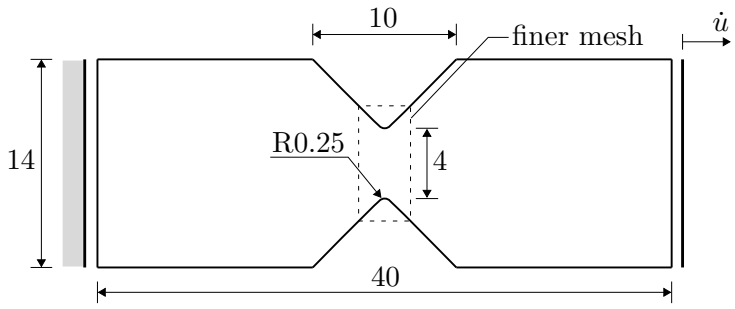

Figure 11: V-notched bar: boundary conditions and geometry and associated dimensions (in mm).

Names	**Values**
Young's modulus (E)	68.9 GPa
Poisson's ratio (ν)	0.33
Hardening law	$\sigma_y(\varepsilon^{\mathrm{p}}_{\mathrm{eq}}) = 700(0.03 + \varepsilon^{\mathrm{p}}_{\mathrm{eq}})^{0.12}$ MPa
Ultimate stress (f_t, f_c)	600 MPa
Fracture energy (G_c)	18 N/mm
Plastic Poisson's ratio (ν_p)	0.5

Table 1: Model parameters for V-notched bar (Al-6061) [26, 27, 28].

In this example, second order elements are used to avoid volumetric locking with the classic Von Mises model. However, linear elements are used for the discretization of the level set field ϕ and the normal velocity v_n because it simplifies the fast marching algorithms.

The geometry of the problem leads to a non-uniform stress state near to the notches. A region around the notches with refined mesh is defined (see Fig. 11) where the effective element size $h = 0.05\,\mathrm{mm}$. The value of $h = 0.05\,\mathrm{mm}$ was determined by carrying out a convergence study in terms of the peak load. In this simulation, the crack growth resistance parameter and, critical length are, respectively, $\eta = 25\,\mathrm{s\,mm^{-1}}$ and $l_c = 0.4\,\mathrm{mm}$. The value of η is determined as fitting parameter. The influence of l_c and η on the response ater choosing l_c based on the model geometry and the mesh size is addressed later.

In Fig. 12, the load-displacement graphs from Li *et al.* [26], Miehe *et al.* [27] and the TLS are drawn together. The results verify the accuracy of the proposed model. The evolution of the damage front is illustrated in Fig. 13.

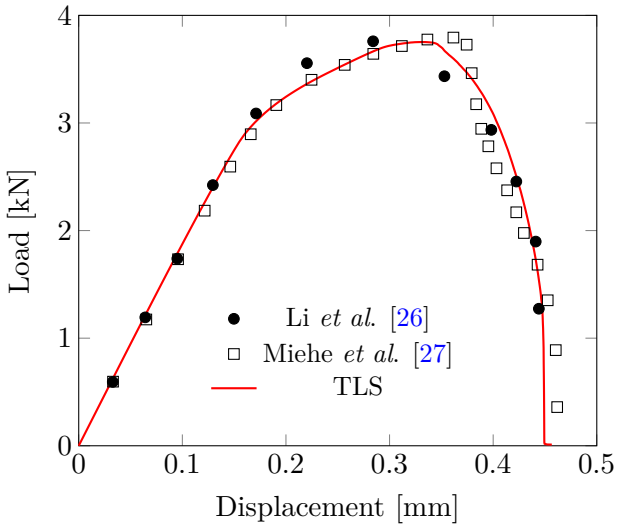

Figure 12: Load-displacement graphs for V-notched bar.

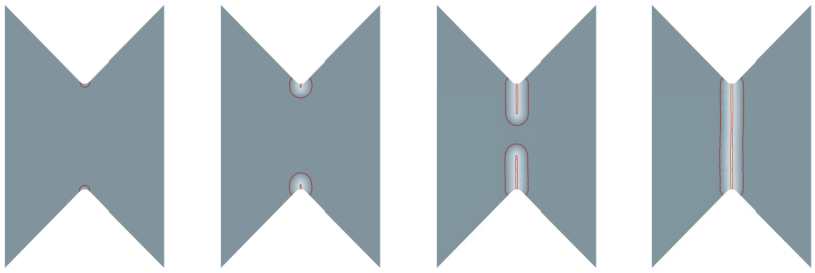

(a) (b) (c) (d)

Figure 13: Evolution of the damage front on V-notched bar at different loading stages: (a) $\approx 3.6\,\mathrm{kN}$, (b) $\approx 3.5\,\mathrm{kN}$, (c) $\approx 2.0\,\mathrm{kN}$ and (d) final failure.

To investigate the influence of l_c on the global response, simulations have been performed with different values of l_c between $0.3\,\mathrm{mm}$ and $0.6\,\mathrm{mm}$ with a fixed value of $\eta = 25\,\mathrm{s\,mm^{-1}}$ and a fixed mesh. Load-displacement curves

from these simulations are shown in Fig. 14. Unlike what was shown in [1, 2], where the global response in terms of load-displacement curves and energy dissipations did not change considerably when varying l_c, for the TLS with linear elastic materials in a quasi-static context, a delayed-failure response for decreasing l_c is observed in the presence of plasticity. This is due to the fact that for small values of l_c, the stress state around the crack tip is higher than the stress state for larger values of l_c, which in turn leads to more plastic strain.

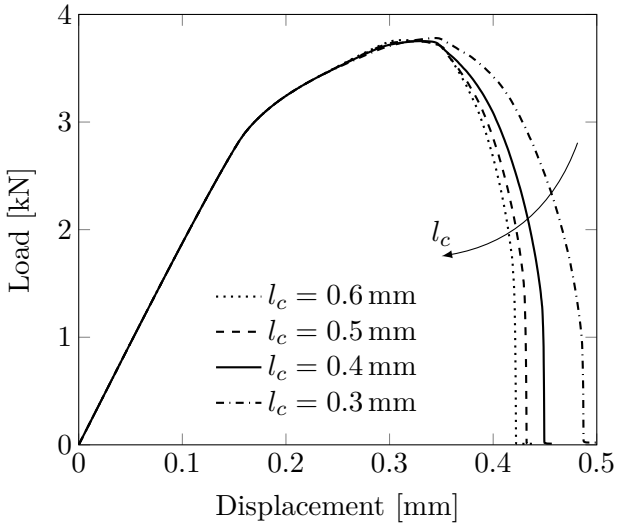

Figure 14: Influence of l_c on the global response. Increasing values of l_c are indicated by the arrow.

To illustrate the effect of the resistance parameter on the post-critical range after damage initialization, the same simulation with $l_c = 0.4\,\mathrm{mm}$ is repeated with values of $\eta = 15\,\mathrm{s\,mm^{-1}}$, $\eta = 20\,\mathrm{s\,mm^{-1}}$, $\eta = 25\,\mathrm{s\,mm^{-1}}$ and $\eta = 30\,\mathrm{s\,mm^{-1}}$. The results are compared in terms of load-displacement curves in Fig. 15. It can be observed that η influences the shape of the post-critical response. As expected, delayed failure behavior is obtained by increasing the value of η. The value of $\eta = 25\,\mathrm{s\,mm^{-1}}$, which gave the good fit in Fig. 12, is clearly in the regime where there is significant influence of η on the response. This means that the actual fracture energy in the simulation is rate-dependent and higher than the G_c from Table 1.

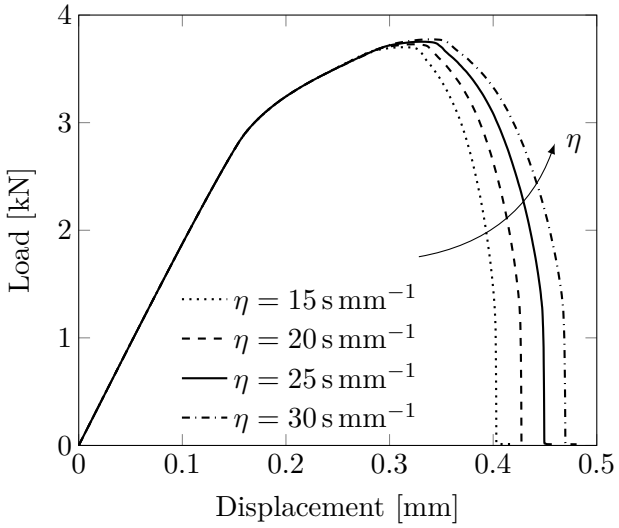

Figure 15: Influence of η on peak response. Increasing values of η are indicated by the arrow.

In order to assess the performance of both mapping operators in a more realistic simulation, once again, a convergence study is carried out. In Fig. 16, the peak load obtained with inverse distance-based interpolation and SPR technique are compared with the result obtained by a reference model in which SPR and $h = 0.015\,\mathrm{mm}$ are used. The same trend is observed that has been presented for the 1D model, in which both operators converge toward the same response with mesh refinement and that the results with SPR are generally more accurate. It is also observed that the mesh with $h = 0.05\,\mathrm{mm}$, which was used in Fig. 12, is suitable since the difference in terms of peak load is negligible.

3.2. Rail shear test

This numerical example is inspired by rail shear test for mode II failure following Van der Meer and Sluys [5]. The case consists of a sandwich with stiff faces and a weak core (see Fig. 17). The faces are loaded in opposite direction so that the core is sheared. This setup mimics the delamination process in composites, where the stiff faces represent the plies or fibers and the core represents the resin-rich region around the interface.

In addition, three different cross-sections are considered as depicted in Fig. 18. These variations in cross-section are identical to those of the specimens that have been tested by Rogers [10] to produce cusp-like features on

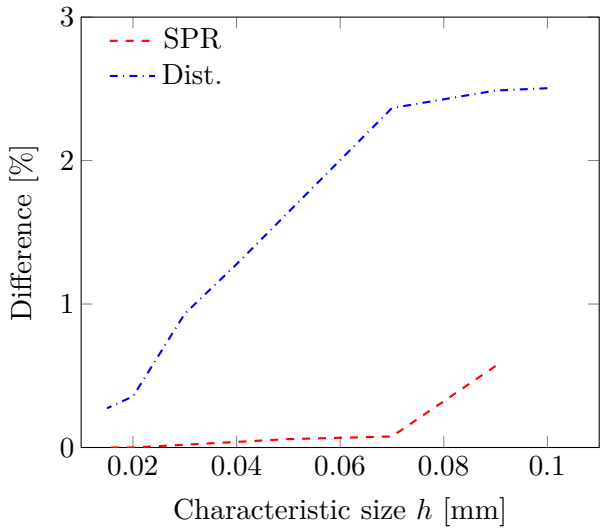

Figure 16: V-notched bar: convergence study for the inverse distance-based operator in terms of peak load.

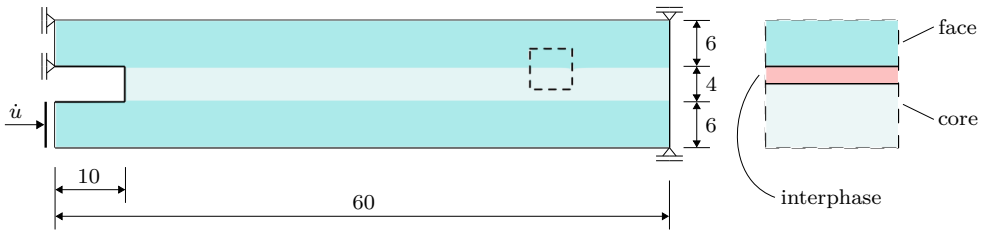

Figure 17: Rail shear test: boundary conditions and geometry and associated dimensions (in mm).

Polyvinylchloride (PVC) foam material. The curvature and width of profiles mimic respectively the influence of fibers radius and the inter-fiber spacing in composites. In the 2D model, the geometry of the cross-section is modeled by varying the model thickness as a function of position.

Young's modulus, Poisson's ratio and fracture energy of the core material are, respectively, $E = 3760\,\text{MPa}$, $\nu = 0.3$ and $G_c = 0.9\,\text{N/mm}$. For plasticity, a plastic Poisson's ratio of 0.39 is used and the fundamental hardening curves are given in Fig. 19 [13, 15]. For the face material, the properties are $E = 200\,\text{GPa}$, $\nu = 0.3$ and $G_c = 9\,\text{N/mm}$. The typical element size h is $0.14\,\text{mm}$ throughout the core and the critical length l_c is equal to $0.6\,\text{mm}$. The distance between a new damage circle and existing damage is set to be

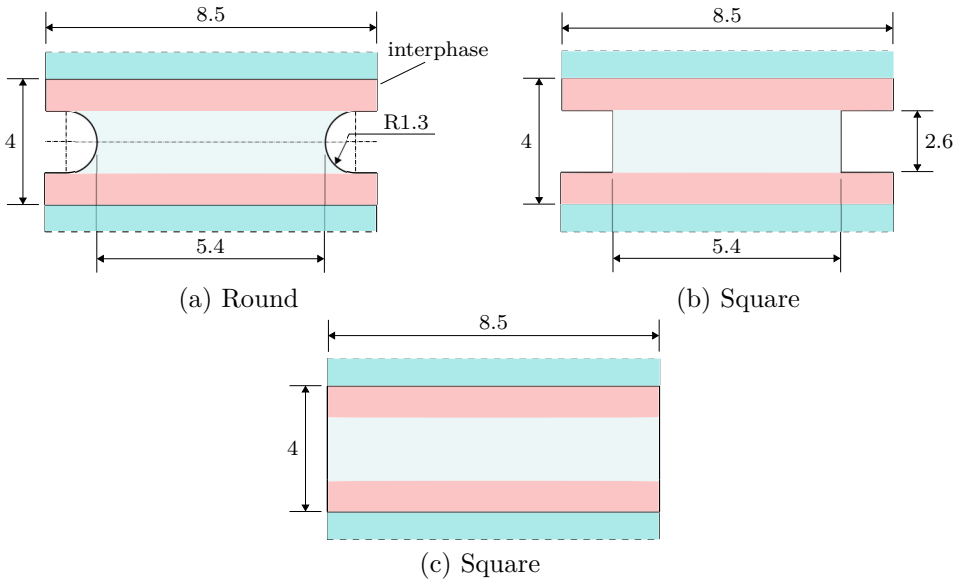

Figure 18: Rail shear test: cross-section profiles (dimensions in mm).

at least 3 mm [5]. The resistance parameter is $\eta = 1\,\mathrm{s\,mm^{-1}}$. Linear elements are used for the discretization of all fields.

When the crack reaches the interface between face and core, sliding deformations lead to one of the principal strains in this zone become negative, in this case the asymmetric constitutive law (Eq. (22)) leads to stiffness recovery and stress transfer across the crack, which is undesired here. In order to guarantee traction-free sliding deformation in this zone, the interphase constitutive law introduced in [5] is applied (see Figs. 17 and 18). This constitutive law makes use of a vector $\mathbf{n}$ normal to the interface and accounts only for stiffness recovery on the strain component along this vector.

First, the difference in response between the proposed model and the earlier TLS model without plasticity for this shear test setup is illustrated by means of load-displacement curves in Fig. 20. Only the round cross-section is considered in this comparison. The difference between the two frameworks in the pre-peak behavior is caused by the added plasticity, while the absence of oscillations in the post-peak behavior is related to the new definition of velocity from Eq. (34).

The framework in [1, 2, 5] is based on a unit load analysis in each time step, which assumes a secant unloading behavior, and allows able to capture snap-backs. The oscillations that are observed in the post-peak response in

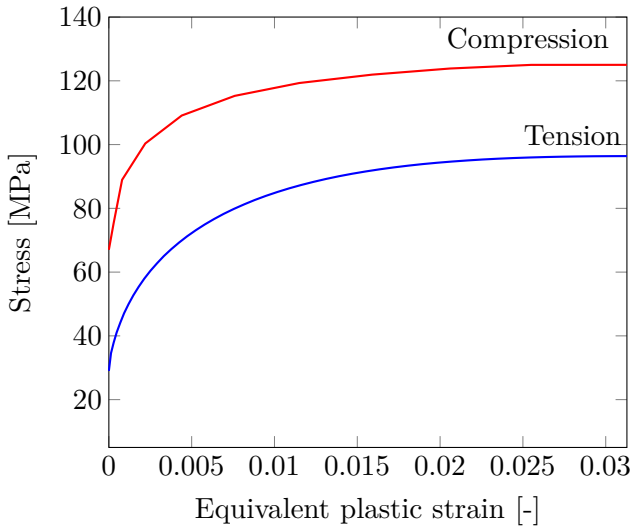

Figure 19: Input hardening curves for plasticity model.

Fig. 20 are related to numerical noise in the maximum value for $\bar{Y}$ that is used to compute the load scale factor such that the scaled maximum value for the configurational force is exactly equal to the material resistance $\bar{Y}_c$. This algorithm based on a unit load analysis and a load scale factor is only applicable to mechanical problems with proportional loading and secant unloading.

Introduction of plasticity in the mechanical problem requires that the computation of displacements is performed at the actual load level. In this sense, the criterion that the configurational force should not exceed the material resistance at any point should be determined iteratively or relaxed by introducing a viscous parameter between front velocity and configurational force, as proposed in this paper, following [16]. The absence of oscillations is a positive side-effect of this change in loading scheme.

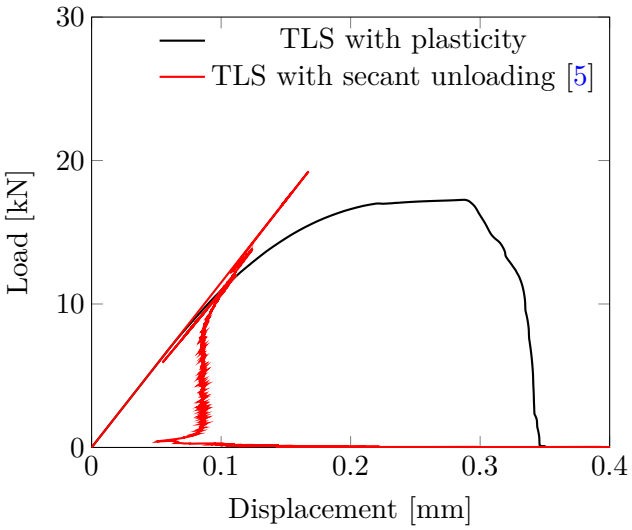

Figure 20: Load-displacement response for current and proposed TLS frameworks in the rail shear test.

The evolution of damage and the equivalent plastic strain distributions for the round cross-section are shown in Fig. 21. It can be observed that damage initiation takes place around the onset of perfect plasticity, first with a single damage spot near the left edge of the soft material and soon after in a series of spaced damage nuclei. As the load increases, all damage nuclei grow to a certain size, until enough energy is available to let a number of inclined cracks grow from these nuclei as the load drops. It is interesting to note that two of the damage spots do not evolve into an inclined crack, which indicates that the numerical spacing does not completely govern the final crack pattern. The same observation was also made in [5] for linear elastic materials. Eventually, the load drops to zero as the inclined cracks coalesce to form a single crack. It can be observed that much of the crack growth takes place in the steep final drop of the load-displacement graph. The adaptive time step according to Eq. (36) ensures that time increments and consequently displacement increments are very small in this phase.

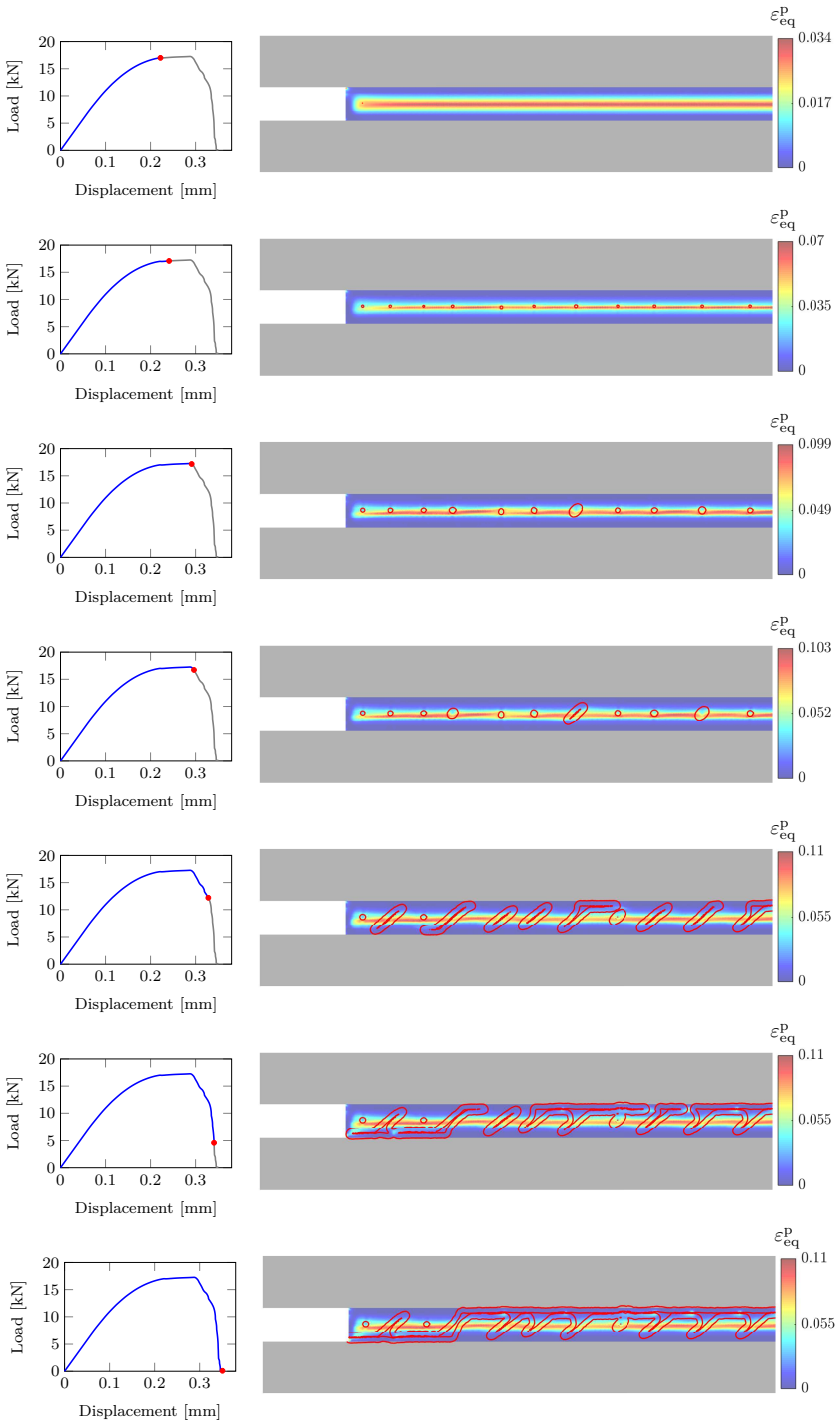

Figure 21: Rail shear test: damage and equivalent plastic strain distributions for the round configuration. The red bullets correspond to some time steps when the time increment size was reduced.

Figures 22 and 23 show the load-displacement curves and final damage distribution obtained with three different cross-sections. It is observed that the change in profile shape has a considerable influence on the fracture morphologies and equilibrium curves. For the round configuration, the number of randomly spaced inclined cracks along the specimen length, which eventually coalesced to form cusps, is larger than for the square and flat configurations. Rogers [10] reported the same trend from experimental observations on PVC foam specimens under similar shear loading conditions. The initial stiffness of the flat specimen is higher than that of the round and square configurations, because of the flexibility that is introduced by side grooving.

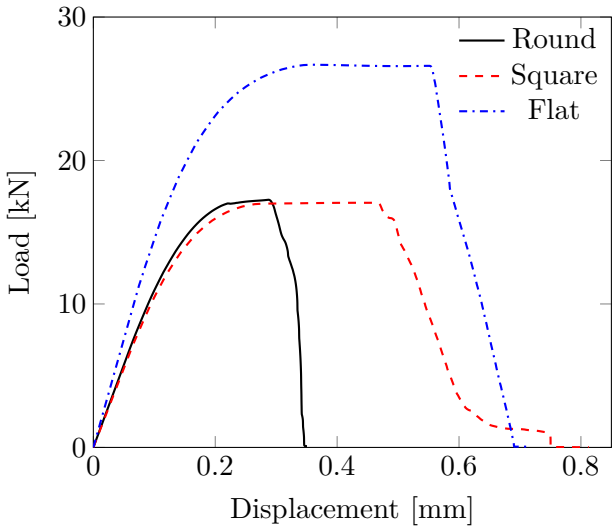

Figure 22: Load-displacements curves for round, square and flat configurations.

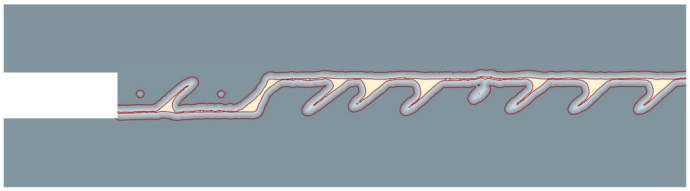

(a) Round

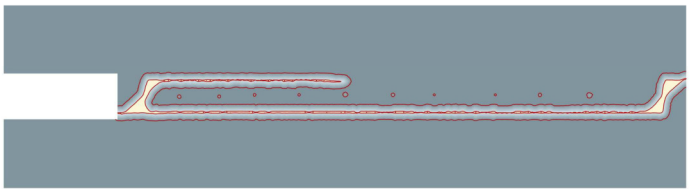

(b) Square

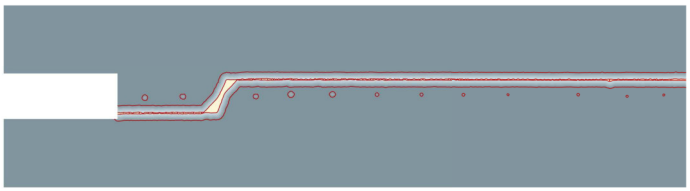

(c) Flat

Figure 23: Rail shear test: final crack distribution for (a) round, (b) square and (c) flat configurations.

4. Conclusion

In this paper, the TLS method for non-local damage modeling has been extended to include plasticity: the elasto-plastic constitutive model for epoxy resin by Melro *et al.* [13] has been combined with the TLS damage formulation, and a new loading scheme to take into account permanent strain has been proposed.

In addition, due to plasticity that bounds stress states, a new criterion for damage nucleation has been developed in order to relate crack initiation under different stress states to a given failure surface. Since the change in the

integration scheme for those elements that are cut by iso-0 and iso-l_c curves, the SPR technique was found to be accurate for transfer of history.

The influence of l_c and η on the global response has been investigated and found to be of similar nature. For a given value of l_c, the optimal value of η has been determined through fitting. In practice, the values from which l_c can be chosen is limited. An upper bound is given by the geometry of the problem at hand, in which the width of the damage band has to be relatively smaller than the geometrical dimensions of the problem. A lower bound for l_c relies on the computational cost, because elements have to be several times smaller than l_c.

The TLS was validated from a good agreement with experimental and numerical results for ductile fracture in a V-notched bar in tension.

The proposed model was successfully applied to the simulation of shear failure including cusp formation. By varying the profile geometry of the core, different load-displacement graphs and fracture morphologies were produced. Cusp development comparable to that in composites was more pronounced in curved-profile configuration, which is in agreement with experimental observations.

Acknowledgment

FM acknowledges financial support from the Netherlands Organization for Scientific Research (NWO) under Vidi grant nr. 16464. LATM acknowledges the financial support by the Federal Institute of Education, Science and Technology of Ceará (IFCE).

References

[1] N. Moës, C. Stolz, P.-E. Bernard, N. Chevaugeon, A level set based model for damage growth: The thick level set approach, Int. J. Numer. Methods Engng. 86 (3) (2011) 358–380.

[2] P. E. Bernard, N. Moës, N. Chevaugeon, Damage growth modeling using the thick level set (TLS) approach: Efficient discretization for quasi-static loadings, Comput. Methods Appl. Mech. Engrg. 233-236 (2012) 11–27.

[3] J. A. Sethian, Level Set Methods and Fast Marching Methods: Envolving Interfaces in Computational Geometry, Fluid Mechanics, Computer

Vision, and Material Science, 2nd Edition, Cambridge University Press, Cambridge, United Kingdom, 1999.

[4] S. Osher, R. Fedkiw, Level Set Methods and Dynamic Implicit Surfaces, 1st Edition, Springer-Verlag, New York, United States of America, 2003.

[5] F. P. van der Meer, L. J. Sluys, The thick level set method: Sliding defomations and damage initiation, Comput. Methods Appl. Mech. Engrg. 285 (2015) 64–82.

[6] K. Moreau, N. Moës, N. Chevaugeon, A. Salzman, Concurrent development of local and non-local damage with the Thick Level Set approach: Implementation aspects and application to quasi-brittle failure, Comput. Methods Appl. Mech. Engrg. 327 (2017) 306–326.

[7] B. Lé, N. Moës, G. Legrain, Coupling damage and cohesive zone models with the thick level set approach to fracture, Engineering Fracture Mechanics 193 (2018) 214–247.

[8] F. Cazes, N. Moës, Comparison of a phase-field model and of a thick level set model for brittle and quasi-brittle fracture, Int. J. Numer. Methods Engng. 103 (2015) 114–143.

[9] A. P. Gómes, N. Moës, C. Stolz, Comparison between thick level set (TLS) and cohesive zone models, Advanced Modeling and Simulation in Engineering Sciences 2 (1) (2015) 18.

[10] C. E. Rogers, Investigating the micromechanisms of mode ii delamination in composite laminates, Engineering, Imperial College London (2009).

[11] E. S. Greenhalgh, C. Rogers, P. Robinson, Fractographic observations on delamination growth and the subsequent migration through the laminate, Composite Science and Technology 69 (14) (2009) 2345–2351.

[12] T. K. O'Brien, Composite interlaminar shear fracture toughness, G_{IIc}: Shear measurement or sheer myth?, Composite Materials: Fatigue and Fracture 7 (1998) 3–18.

[13] A. R. Melro, P. P. Camanho, F. M. A. Pires, S. T. Pinho, Micromechanical analysis of polymer composites reinforced by unidirectional fibres:

Part I - constitutive modelling, Int. J. Solids Struct. 50 (2013) 1897–1905.

[14] E. A. S. Neto, D. Perić, D. R. J. Owen, Computational Methods for Plasticity: Theory and Applications, 1st Edition, John Wiley & Sons Ltd., West Sussex, United Kingdom, 2008.

[15] F. P. van der Meer, Micromechanical validation of a mesomodel for plasticity in composites, European Journal of Mechanics - A/Solids 60 (2016) 58–69.

[16] F. P. van der Meer, N. Moës, L. J. Sluys, A level set model for delamination – modeling crack growth without cohesive zone or stress singularity, Engineering Fracture Mechanics 79 (2012) 191–212.

[17] M. Latifi, F. P. van der Meer, L. J. Sluys, An interface thick level set model for simulating delamination in composites, Int. J. Numer. Methods Engng. 111 (2017) 303–324.

[18] J. Stewart, L. Redlin, S. Watson, Precalculus: Mathematics for Calculus, 6th Edition, Cengage Learning, Belmont, United States of America, 2013.

[19] J. D. Lawrence, A Catalog of Special Plane Curves, 1st Edition, Dover Publications, New York, United States of America, 1972.

[20] G. N. Wells, L. J. Sluys, R. de Borst, Simulating the propagation of displacement discontinuities in a regularized strain-softening medium, Int. J. Numer. Methods Engng. 53 (2002) 1235–1256.

[21] O. C. Zienkiewicz, J. Z. Zhu, The superconvergent patch recovery and *a posteriori* error estimates. Part I: The recovery technique, Int. J. Numer. Methods Engng. 33 (1992) 1331–1364.

[22] O. C. Zienkiewicz, J. Z. Zhu, The superconvergent patch recovery (SPR) and adaptive finite element refinement, Comput. Methods Appl. Mech. Engrg. 101 (1992) 207–224.

[23] J. Shi, D. Chopp, J. Lua, N. Sukumar, T. Belytschko, Abaqus implementation of extended finite element method using a level set presentation for three-dimensional fatigue crack growth and life prediction, Engineering Fracture Mechanics 77 (2010) 2840–2863.

[24] J. C. Simo, T. J. R. Hughes, Computational Inelasticity, 1st Edition, Springer-Verlag, New York, United States of America, 1998.

[25] C. Geuzaine, J.-F. Remacle, Gmsh: A 3-D finite element mesh generator with built-in pre- and post-processing facilities, Int. J. Numer. Methods Engng. 79 (11) (2009) 1309–1331.

[26] H. Li, M. W. Fu, J. Lu, H. Yang, Ductile fracture: Experiments and computations, International Journal of Plasticity 27 (2011) 147–180.

[27] C. Miehe, F. Aldakheel, A. Raina, Phase field modeling of ductile fracture at finite strains: A variational gradient-extended plasticity-damage theory, International Journal of Plasticity 84 (2016) 1–32.

[28] H. Badnava, E. Etermadi, M. A. Msekh, A phase field model for rate-dependent ductile fracture, Metals 7 (5) (2017) 180.